Seven years of Hall thruster modeling: An European collaboration between Bari and Greifswald

IEPC-2007-12

Presented at the 30th International Electric Propulsion Conference, Florence, Italy
September 17-20, 2007

F. Taccogna*, S. Longo† and M. Capitelli‡
Dip. Di Chimica, Universitá degli Studi di Bari & IMIP-CNR, Sect. Bari, via Orabona 4, Bari, I-70126, Italy

and

R. Schneider§
Max-Planck Institute für Plasmaphysik, EURATOM Association, Wendelsteinstr. 1, Greifswald, D-17491, Germany

Different numerical models of the Hall thruster SPT-100 have been developed in the last seven years as result of a collaboration between the IMIP-CNR in Bari and the plasma edge group of the stellarator theory division of the Max-Planck Institute für Plasmaphysik in Greifswald. This European collaboration has benefited from the synergetic interaction of the two groups contributing different know-how in kinetic modelling of cold plasma, magnetic field confinement and plasma-wall interaction. The models represent Particle-in-Cell technique for plasma bulk coupled with Monte Carlo methodologies for collision and boundary modules in the acceleration discharge and hybrid techniques for the plume emitted from the thruster in the near- and far-field regions.

Nomenclature

A	=	area of channel cross section
B	=	magnetic field
c	=	speed of light = 2.9979×10^{8} m/s
e	=	elementary charge = 1.602189×10^{-19} C
E	=	electric field / energy
g	=	relative velocity
H	=	channel width
I	=	current / ionization energy (Xe) = 1.943×10^{-18} J
j	=	radial mesh index / current density
k	=	azimuthal mesh index / wave number / rate coefficient
k_B	=	Boltzmann constant = 1.380662×10^{-23}
L	=	axial length of the channel
m	=	electron mass = 9.11×10^{-31} Kg
M	=	ion mass (Xe) = 2.18×10^{-25} Kg
n	=	density

* Fellowship researcher, Dip. di Chimica, Università degli Studi di Bari, francesco.taccogna@ba.imip.cnr.it.
† Full professor, Dipartimento di Chimica, Università degli Studi di Bari, savino.longo@ba.imip.cnr.it.
‡ Full professor, Dipartimento di Chimica, Università degli Studi di Bari, mario.capitelli@ba.imip.cnr.it.
§ Head of the Helmholtz-Assoc. Junior Res. Group 'Computational Material Science', ralf.schneider@ipp.mpg.de.

r = radial direction
r_L = Larmor radius
r_{in} = inner radius of the channel = 0.03 m
r_{out} = outer radius of the channel = 0.05 m
$rand$ = random number $\in [0,1]$
V_D = discharge voltage
V_d = electron azimuthal drift velocity
z = axial direction
α = electron penetration coefficient
α_d = polarizability
β = Hall parameter
γ = total secondary electron emission coefficient
Γ = integrated total secondary electron emission coefficient
Γ_p = integrated secondary electron emission coefficient induced by bulk primary electrons
Γ_s = integrated secondary electron emission coefficient induced by secondary electrons
δ = true secondary electron emission coefficient
Δt = time step
ε_0 = vacuum permittivity = 8.854188×10^{-12} F/m
ζ = scaling factor <1
η = backscattered electron emission coefficient
θ = azimuthal direction
κ = electron thermal conductivity
λ_D = Debye length
$\mu_\perp$ = cross-field electron mobility
ν = collisional frequency
π = pi-greek = 3.1415926536
ρ = charge density / re-diffused electron emission coefficient
σ = surface charge density / cross section
Φ = electric potential
χ = scattering angle
ω_p = electron plasma frequency
Ω = cyclotron frequency

I. Introduction

The detailed physical picture of the processes in the SPT-100 is very complex[1]. It includes a whole series of phenomena, such as stabilization of the flow in ExB fields, equipotentialization of magnetic lines of force, electron anomalous transport, the so called near-wall conductivity, the dynamic Debye layer with high secondary electron emission yield and the plasmadynamics of the plume. Even nowadays the physical description is far from being complete.

A. The space charge saturated sheath

The presence of an insulator as wall material has a profound effect on the plasma within the Hall channel. After an impact with dielectric walls, high energy electrons are absorbed and release less energetic secondary electrons that are more firmly confined by the magnetic field. The result is that the dielectric wall limits the temperature of the electrons resulting in a smooth continuous variation of the plasma potential and a more efficient ion acceleration. At the same time, the lateral sheath changes its classical character. In fact, under the emission of secondary electrons from the wall, the voltage sheath drop $\Delta\Phi_s$ is given by[2]:

$$\Delta\phi_s = -\frac{k_B T_e}{e} \ln\left[(1-\Gamma)\sqrt{\frac{M}{2\pi m}} \right] \tag{1}$$

where Γ is the integral (over the distribution function of impacting electrons) value of the secondary electron emission coefficient γ. The most important effect of secondary electrons emitted from the wall is to reduce the

voltage drop through the sheath, increasing the number of electrons reaching the wall. However, in SPT the picture becomes much more complex. First, the distribution functions of electrons hitting the surface and secondary electrons emitted from the walls are essentially non-Maxwellian. Second, the electrons in the SPT have energies in the range of 15÷20 eV (necessary to ionize Xe) and most of the ceramics used to made the thruster walls (BN, SiO_2, Al_2O_3) at these energies, have $\gamma \sim 1$. Under these conditions, the classical Debye layer seems to disappear and transform into a non-monotonic behavior (double layer structure). A potential well forms close to the wall which traps a fraction of the secondary electrons (space charge saturation regime). Moreover, for higher electron energies, it loses its static character becoming a structure oscillating in space (extended in a region with size $>>\lambda_D$) and time (on the GHz range), the so called sheath instability[3,4]. Finally, electron-wall interaction is also related to the electron anomalous conductivity.

B. The anomalous electron conductivity

One of the most important open questions in the physics of Hall discharge concerns the electron cross-field mobility. Classical diffusion theory based on collision-induced transport, i.e. electron-neutral collisions ($\mu_\perp \propto B^{-2}$) underestimates the cross-field transport, and numerical models of the discharge usually invoke an adjustable diffusion coefficient to achieve acceptable results. Moreover, the comprehension of this phenomenon is vital for the optimization of this device. The reason for this enhanced cross-field transport is nowadays a subject of considerable and continued debate. However, it is well accepted to attribute the anomalous electron cross-field transport to three different sources.

- *fluctuation-induced transport*: this kind of diffusion can be divided into two classes which depend on the character of the fluctuating azimuthal electric field[5]. Denoting the k^{th} Fourier space component of the electric field by $E_k=|E_k|exp[i\varphi_k(t)]$, in one case $\varphi_k(t)$ is a statistical function of time and the anomalous diffusion coefficient depends on the correlation time of the electric field fluctuations[6], while in the second case, the electric field is made up of a superposition of coherent waves $\varphi_k(t)=-\omega t+k_\theta\theta$ and the anomalous diffusion arises from a resonance of particles and waves which move along θ with the same velocity $v_{phase} \approx V_d$. For this reason, one is interested in high frequency (1÷50 MHz) short wavelength oscillations in the plasma properties, which have been already detected from experiments[7-11], numerical model[12,13] and linear stability analysis[14-19]. The origin of these HF fluctuations is certain types of instabilities, among which the most probable candidates are:

a) microinstabilities (sheath[3,4], stream or anisotropy[20]);

b) resistive instability[15] (electrostatic lower hybrid waves) due to the coupling with the electron drift flow in the presence of electron collisions;

c) axial gradient-driven instability[16] (identified also as Rayleigh-type instability) detected at the axial location where the following condition is fulfilled:

$$\Omega_e \frac{\partial}{\partial z}\left(\ln\frac{B}{n}\right) + c\frac{\partial^2 V_d}{\partial z^2} = 0 \tag{2}$$

d) electron drift instability[19] based on the resonance between $k_\theta V_d$ and the cyclotron harmonics $n\Omega_e$ in the frequency range $\Omega_i << \omega << \Omega_e$, occurring for very short wavelengths close to or even below the electron gyroradius r_L.

The anomalous axial electron current results from the phase angle correlation γ between the azimuthal electric field and the density fluctuations[21] (neglecting the axial component of the magnetic field):

$$j_{ez,fit} = en_e\frac{E_\theta}{B_r} \cong -ek_\theta\frac{\tilde{n}\tilde{\phi}}{B_r}\sin\gamma \tag{3}$$

which leads to a Bohm-type[22] anomalous conductivity $\mu_\perp \propto B^{-1}$;

- *wall-induced transport*: the electron-wall interactions (the so called near-wall conductivity NWC[23,24]) leading to a non-specular reflection or emission of electrons which leave the walls following another spiral trajectory displaced toward the anode. This creates a classical conductivity varying like B^{-2}:

$$j_{ez,wit} = 2\frac{m}{e}\frac{n}{H}\sqrt{\frac{kT_e}{M}}\frac{E_z}{B_r^2}\frac{\Gamma}{1-\Gamma} \tag{4}$$

that does not justify the high axial electron current measured. In reality, the NWC is a more complex phenomenon including in nonlinear way numerous effects:
a) secondary electron beam emitted from the wall and inducing secondaries on the opposite wall[24] (Γ is substituted in eq. (4) by an effective value $\Gamma_{eff}=\Gamma_p/[1+\alpha(\Gamma_p-\Gamma_s)]$);
b) macroroughness on the surface[25];
c) ion-wall recombination[26] leading to an additional correcting factor $2\sqrt{(T_e/T_N)}$ in eq. (4);
d) photoelectron emission from the wall due to UV radiation[27];
e) sheath oscillations as recently demonstrated by Monte Carlo calculations[28].
- *gradient-induced transport*: non-local effect due to small length scale of gradients leading to a distortion of the gyro-motion, known as neoclassical conductivity.

Recently[29] it has been suggested that the general belief that Bohm-like anomalous conductivity was dominant outside the thruster channel whereas electron-wall conductivity prevails inside the channel is not valid. It has been concluded that only the plasma azimuthal fluctuation is responsible for anomalous "collisionless" electron transport inside and outside the Hall thruster channel. Nevertheless, changing the wall material of Hall thrusters results in significant plasma parameters and electron axial current changes[30-32]. Then, there are strong arguments to conclude that the azimuthal fluctuations could be induced by surface effects. Finally, concerning the neoclassical gradient-induced transport, it has been demonstrated to have a negligible effect on the enhancement of the electron axial current inside the thruster channel[33].

C. Plasmadynamics of the plume: near- and far-field regions

A major concern in the use of SPT-100 is the possible damage their plumes may cause to the host spacecraft and to communication interference of satellites. Indeed, SPT-100, in operation produces, besides high energy ions and electrons emitted to neutralize the positive space charge, also neutral unionized propellant atoms and low energy ions created by charge exchange (CX) collisions between ions and atoms in which electrons are transferred or by electron impact ionization of neutral atoms. These particles are more influenced by the self-consistent electric fields that cause slow ions to propagate radially (reducing the efficiency) and to flow upstream, while gaining energy. Finally, a very important region is the very-near-field region of the plume (up to 10 cm from the exit plane). In fact, in this region, there are many new aspects to take in account as plasma-wall interaction, magnetic field effect, non isothermal electrons, electron-neutral collisions, cathode location, *etc*.

II. Numerical Models

The complexity, up to the kinetic level, of the physics of SPT, in addiction to the experimental difficulties in the investigation of such a small and surface-dominated plasma device and the ability to simulate a wider variety of external ambient conditions, makes the use of numerical experiments[34,35] a fundamental tool in understanding and optimizing this thruster.

Models of Hall thrusters have been developed using fluid[36-38] and hybrid fluid-particle approaches[39-42]. A question which cannot be resolved by these models, and which in fact strongly limits the reliability of their results, is the strong departure from the Maxwellian distribution of electrons (due to low collisionality), the electron transport, and the important role of electron-wall interaction. As a result, SPT performance is affected by both the state of the wall surface and the properties of plasma structures on Debye and electron-Larmor scales. Therefore, the construction of a self-consistent theory of SPT processes requires a kinetic description of not only heavy particles (atoms and ions), but of electrons as well. The ideal numerical model would be a particle model for all the species in three dimension. Nowadays, such a model is unpractical because it would need too large considerable amount of computation time. This is because, in particle models, the time step must be smaller than the plasma period ($\sim 10^{-11}$ s in our case) while to reach steady state the system needs more than hundreds of microseconds (the transit time of a neutral atom), and the mesh cell size must be smaller than Debye length. In order to keep the fully kinetic character of the model, it is necessary to reduce the dimensionality of the system, limiting the domain to one or two dimensions.

A. 2D(r,z) model of the channel: geometrical scaling

Nevertheless, additional tricks are necessary in order to speed up the execution of the code. Previous fully kinetic PIC codes used an artificial electron to ion mass ratio[43] and/or an artificial vacuum permittivity constant[44]. The smaller heavy particle mass, for speeding up the neutrals and ions, decreases the number of iterations necessary to

reach convergence, but at the same time it changes the ratio between electron and ion current, a fundamental parameter for the anomalous electron transport and thruster efficiency, modifying completely the discharge characteristics. The larger permittivity constant decreases the plasma frequency and increases the Debye length, hence the computational time step and the required grid cell size increase. This trick changes dramatically the peculiar space and time scales of the plasma state making it impossible to recover the original system.

Our proposal in the 2D(r,z)[45-50] model is based on the reduction of the geometrical dimension of the thruster preserving more rigorously the values of the relevant parameters governing the physics of the discharge. This creates a more self-similar copy of the original system[51]. All the basic plasma characteristics in Hall discharge devices rely heavily on the ionization process and on the electron confinement scheme, therefore during the channel reduction the Knudsen and Hall parameters must remain unchanged:

$$\frac{\lambda_{eN}}{L} = const\ ;\ \ \frac{\omega_p}{\nu_{eN}} = const\ ;\ \ \frac{r_{L,e}}{L} = const\ ;\ \ \frac{\omega_p}{\Omega_e} = const \tag{5}$$

From the first relation, it follows that the density scales as the inverse of the length of the system (we assume no scaling of cross sections):

$$n \sim 1/L \tag{6.a}$$

The second relation guarantees the conservation of electron-neutral collision probability during the reduction. This involves the scaling of electron velocity according to the following law:

$$v_e \sim \sqrt{L} \tag{6.b}$$

In order to have ion velocity scaled as electron one, the applied voltage now scales as

$$V_d \sim L \tag{6.c}$$

From the third constraint it follows the scaling of magnetic field:

$$B \sim \sqrt{1/L} \tag{6.d}$$

The last relation of eqs. (5) is automatically verified. Scaling relations for the self-similar copy of the acceleration channel are summarized in Table I.

The total simulation time (on the order of neutral transit time T_N) scales linearly with the length of the channel, while the time step Δt_e, as imposed by the stability criterion of the numerical method used to integrate the equations of motion, scales as the plasma oscillation period, that is with the inverse of the square root of the density. Therefore, reducing the linear dimension L of the discharge by a factor $\zeta \in [0,1]$, it leads to a reduced number of PIC cycles N_{PIC} necessary to reach a steady state given by:

$$N_{PIC} = \frac{T_N}{\Delta t_E} \approx L\sqrt{n} = \zeta^{1/2} N^*_{PIC} \tag{6}$$

where the asterisk is referred to the un-scaled system.

The Debye parameter is conserved: $\lambda_D/L \sim 1$. This results in no reduction in the number of mesh cells necessary to cover the entire domain, and keep the physics of plasma-

Quantities	Scaling Laws
Length	$L=\zeta L^*$
Particle density	$n=\zeta^{-1} n^*$
Electric potential	$V=\zeta V^*$
Electric field	$E=E^*$
Magnetic field	$B=\zeta^{-1/2} B^*$
Mass flow rate	$\dot{m}=\zeta \dot{m}^*$
Velocity	$v=\zeta^{1/2} v^*$
Current	$I=\zeta^{3/2} I^*$
Temperature	$T=\zeta T^*$
Thrust	$F=\zeta^{3/2} F^*$
Specific impulse	$I_{sp}=\zeta^{1/2} I^*_{sp}$
Efficiency	$\eta=\zeta^{-1} \eta^*$

Table I. Scaling laws of the self-similar system[51] (un-scaled quantities are designed with asterisk).

wall transition unchanged. Moreover, the ratio of plasma frequency to electron cyclotron frequency is also conserved. This is an important parameter for the plasma fluctuation dynamics in magnetic confinement systems. Its conservation guarantees a correct evaluation of UHF oscillations inside the channel and the related anomalous electron transport.

In addition to the reduction of the number of total PIC cycles, the number of real particles in the scaled system $N_{p,real}=nVol=\zeta^2 N_{p,real}^*$ is reduced, allowing a better statistics in the simulation. Nevertheless, limitations in the geometrical reduction are necessary. First, the plasma parameter N_D, the number of particles in a Debye sphere, is unavoidably reduced, leading to plasma crystalization. As it is well known, PIC validity is based on the requirement that collective effects are dominant over the collisional one, that is:

$$N_D >> 1\,; \quad \frac{\ln N_D}{N_D} << 1 \tag{8}$$

Furthermore, the ratio between surface and volume is unavoidably changed leading to the possible increasing of the surface effects (*i.e.* secondary electron emission) in the reduced system. Finally, gradient-driven instabilities could appear due to the fact that some quantities scale differently from the size of the system.

Before the simulation (domain reported in Fig. 1) begins, we fix all the parameters that remain constant during the execution. In particular, the magnetic field and the neutral distribution. Indeed, magnetic field variations due to plasma currents and changing electric fields are small compared to the field produced by the electromagnets. For the radial component of the magnetostatic field profile we have chosen the bell-shaped expression:

$$B_r(r,z) = B_0 \frac{r_{in}}{r} e^{-16(z/L-1)^2} \tag{9}$$

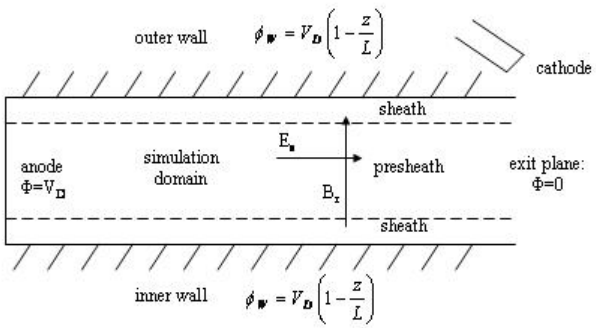

Figure 1. Sketch of the 2D(r,z) simulation domain.

while the axial component has been neglected. We initialize the simulation by expanding a plume of neutrals from the anode until we approach a steady state. Neutral macroparticles are injected (according to the scaled value of the mass flow rate Tab. I) with a radial position sampled from an uniform cylindrical density distribution and their initial velocity distribution is taken to be half-Maxwellian with a temperature $T_n=1000\ K$. Neutrals disappear when they reach the right boundary of the geometry, while when they hit the anode and walls are re-emitted according to an half-Maxwellian at a wall temperature $T_w=700\ K$. The probability densities for axial and azimuthal velocity components are Gaussian distribution, while the probability density for the radial component is a Rayleigh distribution. Neutral-neutral collisions may be ignored, assuming a neutral free molecular regime.

When neutral particles have filled the simulation region, the PIC module is called. Due to very different time scales of electrons and heavy particles, an explicit subcycling scheme[52] is used in which electrons equation of motion and Poisson's equation are solved every electron PIC cycle, while ions and neutrals are moved each $\Delta t_i=5\Delta t_e$. The electric field felt by the ions is filtered (a simple time average of the electric fields seen by the electrons works well). Since the simulation starts from the scratch, we use, instead of a fixed time step, an adaptive time step: $\Delta t_e=0.8/\omega_p$. Every electron PIC-cycle, cathode electrons are introduced at the free space right boundary (the cathode is not included in the simulation region) according to a cylindrical radial distribution in position and a half-Maxwellian distribution with a temperature $T_e=15\ eV$ (scaled according to the law reported in Tab. I) in velocity. The amount of electrons to be introduced is determined through the steady-state current control method of electron injection[44]:

$$\Delta N_e = \frac{I_d \Delta t_e}{ew} - \Delta N_{i,C} + \Delta N_{e,C} \tag{10}$$

where $\Delta N_{i,C}$ and $\Delta N_{e,C}$ are the number of ions and electrons, respectively, passing the free space boundary each electron iteration.

Verboncoeur interpolation method[53] which guarantees charge density conservation on a radial metrics is used to weight particles to the grid nodes, where the field equations are solved, and to weight the fields back to the particles. Poisson equation:

$$\left(\frac{\partial^2}{\partial r^2}+\frac{1}{r}\frac{\partial}{\partial r}+\frac{\partial}{\partial z^2}\right)\phi(r,z)=-\frac{\rho(r,z)}{\varepsilon_0} \tag{11.a}$$

is solved iteratively using Successive Over-Relaxation (SOR) with Chebyscev acceleration technique[34]. As regards the boundary conditions, we keep the electric potential constant at the anode and at the exit plane:

$$\phi_A = V_d \tag{11.b}$$

$$\phi_C = 0 \tag{11.c}$$

while at the dielectric surface a simplified fixed linear decay is imposed:

$$\phi_W = V_D\left(1-\frac{z}{L}\right) \tag{11.d}$$

Electrons are moved discretizing the equations of motion by the Boris-Buneman leapfrog method[35]. All electrons which hit the anode boundary, the lateral walls and the free space boundary are deleted. An ion which impacts the anode and the walls disappears, but particle and energy flux are computed and used to estimate the sputtering yield using the Monte Carlo code SDTrimSP[54]. At the free space boundaries, all particles are deleted and a count of electron, ion and neutral fluxes is maintained.

After each electron collisionless stage a Monte Carlo Collision (MCC) routine is called. We apply the standard "null collision" technique[55,56] to simulate electron-neutral collisions, which include elastic scattering, excitation, and single ionization (for the set of cross sections used see Ref. 44). Following Ref. 57, the probability distribution function for the electrons produced in the ionization is taken to be:

$$f(E_p,E_s)=\frac{\alpha\sigma_i(E_p)}{(\alpha^2+E_s^2)\arctan\left(\dfrac{E_p-I}{2\alpha}\right)} \tag{12.a}$$

where the parameter α is set to 8.7 eV, while the angular electron scattering for all the types of electron-atom collisions is taken from the following distribution:

$$f(E_p',\chi)=\frac{E_p'}{4\pi\left[1+E_p'\sin^2(\chi/2)\right]\ln(1+E_p')} \tag{12.b}$$

where E_p' is the post-collisional energy of the primary electron. Electron energy loss associated with elastic electron-atom collisions is neglected. For simplicity, only one excitation collision has been considered. Upon excitation of a neutral Xe atom, the electron is assumed to lose energy of 8.32 eV. Anyway, the excited states kinetics is not included, considering the quenching of excited states instantaneous.

B. 1D(r) model of the acceleration region: secondary electron emission

In the previous model, a simplified boundary conditions for particle and field were implemented on the lateral walls. In fact, condition (11.d) does not correspond to a floating wall and it represents a strong approximation. In order to take into account the important nature of secondary electron emission and floating potential condition of the dielectric lateral wall a 1D(r)[58-62] model of the acceleration region of the discharge has been developed. The simulation has been done per unit length in transverse direction for axial-symmetry (azimuthal gradients are neglected). The "local-field approximation" is applied neglecting the effects of axial gradients based on the fact that

all the axial gradient lengths $L_{\nabla f} = \left|\partial \ln f / \partial z\right|^{-1} \sim 1\ cm$ are larger than the characteristic lengths of the system (λ_D, r_L, ionization mean free path and energy relaxation length) and the radial gradient length. Indeed, in the acceleration part of the channel, the electron radial dynamics is much faster than the axial one due to the radial magnetic field impedance. The residence time for electrons in the acceleration region is estimated to be $\sim 10^{-5}\ s$. Concerning the ions, the situation is completely different, because their dynamics is mostly axial and radial. Ions are created by ionization and lost by wall recombination and axial upstream flow (toward the exit plane). Therefore, the total simulation time has to be limited to the ion residence time in the acceleration region estimated to be $T_i \approx 5\ \mu s$. In order to keep high the statistical quality of the simulation a non-uniform radial grid is implemented. Due to cylindrical metrics, in order to have a constant volume, the radial cell size must be proportional to the radial position:

$$\Delta r(j) = \left(\sqrt{j} - \sqrt{j-1}\right)\Delta r(1) \qquad j = 2,..., N_r \tag{13}$$

where $\Delta r(1) = H/\sqrt{N_r}$. In this way, the average number of particles per cell varies between $5 \div 100$. The timestep is chosen such that $\omega_p \Delta t = 0.3$. Realistic values of the ion mass and vacuum permittivity are kept.

The prescribed values used as input parameters, characteristic for the acceleration region, are: neutral density $n_N = 2x10^{18}\ m^{-3}$ (neutral dynamics is not considered and neutrals are treated as a fixed background); axial electric field $E_z = 10^4\ V/m$; radial magnetic field $B_{r,in} = 150\ Gauss$ (non-uniform, see eq. (9)). The simulation starts with a uniform distribution of electrons and ions along the radial domain with a density $n_p = 0.8x10^{17}\ m^{-3}$. Velocities are sampled from a Maxwellian distribution with initial temperatures $T_e = 1\ eV$ and $T_i = 0.1\ eV$. The discharge is self-sustained with electrons created by bulk ionization and surface emission. The contribution from the cathode neutralizer is neglected due to the fact that in the acceleration region the current is carried mostly by ions. The Poisson equation in cylindrical radial coordinate r:

$$\left(\frac{\partial^2}{\partial r^2} + \frac{1}{r}\frac{\partial}{\partial r}\right)\phi(r) = -\frac{\rho(r)}{\varepsilon_0} \tag{14.a}$$

is discretized and solved directly using the Thomas tridiagonal algorithm[63]. For this purpose, a fixed Dirichelet boundary condition $\Phi_{wo} = 0\ V$ is used at the outer wall in order to reproduce the external cathode position, while the inner surface can float electrically with respect to the plasma such that the total current $I = I_i - I_e$ to the surface is zero (zero-current condition). The electric field (Neumann condition) at the wall is proportional to the net charge σ_{wi} which has accumulated on the surface (the possible surface conductivity of the dielectric is neglected):

$$\left.\frac{\partial \phi}{\partial r}\right|_{wi} = E_{r,wi} = -\frac{\sigma_{wi}}{\varepsilon_0} \tag{14.b}$$

The same bulk collision methodology of the 2D(r,z) model is used, while concerning the boundary module, when an electron strikes the dielectric wall, a Monte Carlo probabilistic model[64-68] is used which allows a detailed dependence of the secondary electron emission coefficient SEY on the primary electron energy. In fact, we choose the number of electrons emitted based on its energy E_p. It is distinguished between three different type of secondary electrons (see Fig. 2): backscattered (high energy region), re-diffused (middle energy region) and true secondary electrons (low energy region). The fine structure of SEY is very important at the energies typical of SPT operation ($<30\ eV$). Theoretically, the backscattering coefficient η (red curve) should grow with the decrease of incident electron energy (~ 0.8 at $0\ eV$), while the yield of re-diffused ρ and true secondary δ electrons (green and blue curves) decreases and reaches zero. The superposition of the different contributions γ (black curve) has a distinguishable minimum in the low energy region ($\sim 5\ eV$, as recently shown from experiment[65]), which can not be reproduced by the common used linear or power fit of SEY[27,71]. Concerning the angular dependence of SEY, it is neglected due to the energy range considered[43]. For simplicity, we assume the same emission-angle distribution ($\sim \cos\theta$ and uniform φ angle) for all electrons, regardless of the physical mechanism by which they were generated. Secondary electrons are generated instantaneously when a primary electron hits the surface, since the time lag of secondary emission is estimated to be $10^{-13} \div 10^{-14}\ s$, i.e., much shorter than any time scale relevant to the plasma dynamics inside the SPT channel. Finally, when an ion strikes the wall it is neutralized and deleted. Ion-induced secondary electron emission becomes an important event only at KeV energy range.

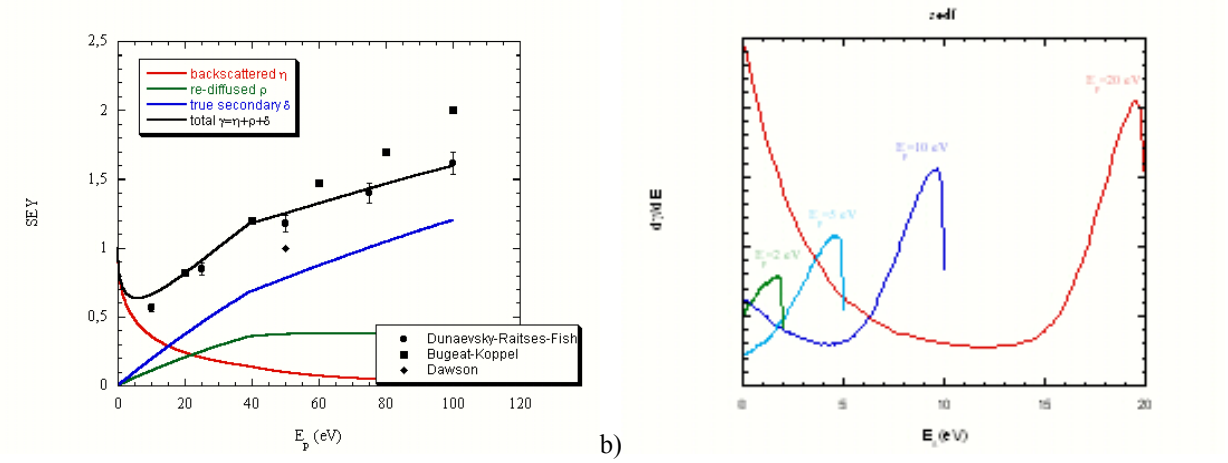

a) b)

Figure 2. (a) The three contributions η, ρ and δ of total secondary electron emission coefficient γ (SEY) as a function of the impact electron energy E_p (measured data[69-71] are also reported). (b) secondary electron distribution function sedf for four different electron primary energies: E_p=2, 5, 10 and 20 eV. Data are for BN as wall material.

C. 2D(r,θ) model of the acceleration region

Up to now, only Hirakawa and Arakawa[12,13], Adam *et al.*[72] and Fernandez *et al.*[73] modelled the azimuthal behaviour, but the radial contribution was missing or a hybrid model (electrons are treated as fluid with a prescribed fixed temperature) was used. Here, a model of the radial and azimuthal direction is developed at the same time in order to capture self-consistently the evolution of the azimuthal disturbance and the secondary electron emission from the wall without use of *ad-hoc* parameters for the axial transport mechanism. The axial location investigated is the acceleration region of the thruster, where both, a large drift velocity responsible for the instability and a strong secondary electron emission from the wall are present. Indeed, experimental measurements[74] show in this region a pronounced deviation of the Hall parameter $\beta=j_{e,\theta}/j_{e,z}$ from both the classical and Bohm value. The simulation[75] represents an azimuthal extension of previous radial models. The domain (Fig. 3), unit length per axial z direction, consists of a cross section of the annular channel. In order to lower the computational cost we have reduced the periodicity length to 1/16 of the entire azimuthal domain. We have checked that this does not affect the results in which we are interested. In fact, as the system is periodic in the θ direction, the length of the simulation determines the modes which are allowed to develop if they are unstable. A recent linear stability analysis[19] has shown that the fundamental mode $k_\theta V_d/\omega_p=0.515$ and its first harmonic $k_\theta V_d/\omega_p=1.03$ are unstable, while next harmonics are outside the unstable lobes or might be unstable with a negligible growth rate. Therefore, our simulation domain size is large enough to capture the relevant instabilities.

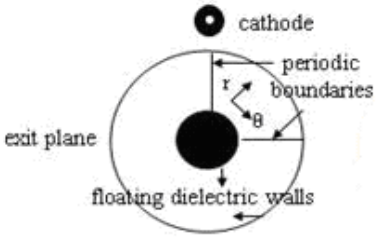

Figure 3. Sketch of the 2D(r,θ) simulation domain.

The same input parameters, initial conditions, MCC and SEE module of the 1D(r) model are used. In this case, the Poisson equation:

$$\left(\frac{\partial^2}{\partial r^2}+\frac{1}{r}\frac{\partial}{\partial r}+\frac{1}{r^2}\frac{\partial^2}{\partial \theta^2}\right)\phi(r,\theta)=-\frac{\rho(r,\theta)}{\varepsilon_0} \qquad (15)$$

is discretized and solved by the direct method of cyclic reduction[76] using the same boundary conditions on the lateral walls and periodicity on the azimuthal boundaries.

D. 2D(r,z) hybrid models of the plume

For the far-field region of the plume emitted from the thruster, the physical domain considered is 2D(r,z) axisymmetric, enclosed in a rectangular numerical domain (1.5 m X 1.2 m) complicated by the presence of the nozzle shape on two sides (see Fig. 4)[77-79]. The model includes three species: electrons, Xe^{+} and Xe^{++} ions (10% of doubly ionized ions at the inlet). It is hybrid: ions are treated as particles and loaded into the simulation at each time step from the exit plane. The ion exit conditions (radial position and velocity components) are given on the basis of fitted experimental data[80]. Electrons are included by a quasi equilibrium ansatz assuming a fluid Boltzmann barometric relation:

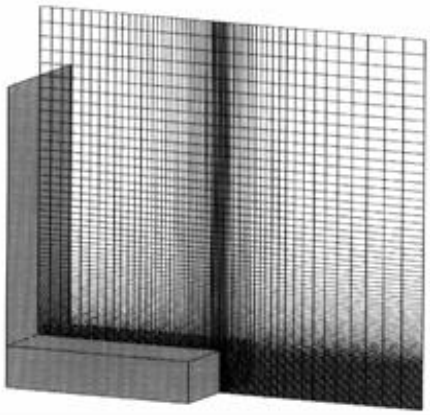

Figure 4. Sketch of the 2D(r,z) simulation domain of the far-field region of the plume.

$$n_e(r,z) = n_{ref} \exp[e(\phi(r,z) - \phi_p) / k_B T_e(r,z)] \qquad (16)$$

but not isothermal electron component. The Poisson adiabatic equation (the electrons are assumed to act as an expanding fluid at isentropic conditions) is used:

$$T_e(r,z) = T_{ref} \left(\frac{n_e(r,z)}{n_{ref}} \right)^{2/3} \qquad (17)$$

where the constants n_{ref}, T_{ref} are chosen to closely match the measurements[81]. The corresponding Poisson equation is highly nonlinear:

$$\nabla^2 \phi(r,z) + \frac{\rho_i(r,z)}{\varepsilon_0} - \frac{\rho_{ref}}{\varepsilon_0} \exp[e(\phi(r,z) - \phi_p) / k_B T_e(r,z)] = 0 \qquad (18)$$

and it is linearized with the Newton-Raphson method[34] and solved with SOR technique. The grid is non-uniform in both r and z coordinates in order to adapt in a simple and straightforward way to the local plasma density (see Fig. 4). Since the grid cell size should be on the order of λ_D which scales with plasma density as $\sqrt{n}$, the grid is linearly stretched in the r and z directions from the thruster exit to follow the increase in Debye length due to the density decrease which is assumed to decay as $1/(r+z)^2$ from the exit plane.

The important ion-neutral collisional processes (momentum MX and charge exchange CX) are modeled using the Test-Particle Monte Carlo method of Nanbu and Kitatani[55,82] which is based on an attractive polarization potential with a rigid core between the neutral and ion parent particle:

$$U(r) = -\frac{\alpha_d e^2}{2(4\pi\varepsilon_0)^2} \frac{1}{r^4} \qquad (19)$$

This assumption corresponds to a dipole-induced dipole interaction. As a consequence, there are two types of orbits: for impact parameters $b > b_L = \left(\frac{8\alpha_d e^2}{(4\pi\varepsilon_0)^2 M g^2} \right)^{1/4}$, the orbit has a hyperbolic character, while for $b<b_L$, the incoming particle is "captured" and the orbit spirals into the core, leading to a large scattering angle.

With the assumption of a rigid core size r_c equal to the radius of the limiting circle $r_L=b_L/\sqrt{2}$, the deflection angle χ is given by:

- if $\beta=b/b_L<1$ the scattering in the rigid core is considered isotropic, then:

$$\cos\chi = 1 - 2\,rand\ ; \qquad (20.a)$$

- if $1<\beta<3$,

$$\chi(\beta) = \pi - \sqrt{\frac{8}{1+\sqrt{1-1/\beta^4}}}\, F\left(\frac{\pi}{2}, \sqrt{\frac{1}{2\beta^4 + 2\beta^2\sqrt{\beta^4-1}+1}}\right) \tag{20.b}$$

where $F(x,y)$ is the elliptic integral. This equation is solved numerically and a tabulation of values is prepared in advance to use a linear interpolation.
- if β>3 the following asymptotic expansion of (20.b) is used

$$\chi(\beta) = -\frac{3\pi}{16}\beta^{-4}. \tag{20.c}$$

To avoid divergence, a non-dimensional impact parameter cut-off $\beta_\infty=15$, for which χ is negligibly small, is introduced.
The charge exchange process is modeled assuming that the probability of this event is $P_{cx}=1/2$ for $b\le b_{cx}$ and $P_{cx}=0$ for $b>b_{cx}$, where $b_{cx} = A\left(\frac{2\alpha_d e^2}{(4\pi\varepsilon_0)^2}\right)^{1/4}$, that is the charge exchange cross section is considered constant.
The neutral density and temperature are assumed to remain constants.
Concerning the near-field region, the simulation domain[83] has a simpler structure (0.2 m X 0.2 m) and in order to take into account the magnetic field effect in the electron fluid representation, the general electron momentum conserving equation is considered. Neglecting the unsteady (on ion time scale), inertial (the electrons cannot leave a region in a large group without a large charge imbalance) and collision drag terms (the ratio of the collision frequency to the plasma and cyclotron frequency is much less than *1*) and differentiating, it results:

$$\nabla^2\phi = \mathbf{B}\cdot\nabla\times\mathbf{v}_e + \frac{k_B T_e}{e}\nabla^2 \ln\rho_e + \frac{k_B}{e}\nabla^2 T_e + \frac{k_B}{e}\nabla\ln\rho_e\cdot\nabla T_e \tag{21.a}$$

Equating the right hand side of this equation to the source term of Poisson equation, the following differential equation for the electron charge density results:

$$\frac{k_B T_e}{e}\nabla^2 \ln\rho_e + \frac{k_B}{e}\nabla\ln\rho_e\cdot\nabla T_e - \frac{\rho_e}{\varepsilon_0} - B_r\frac{\partial v_{e,\theta}}{\partial z} + \frac{k_B}{e}\nabla^2 T_e + \frac{\rho_i}{\varepsilon_0} = 0 \tag{21.b}$$

where the electron azimuthal velocity is set equal to

$$v_{e,\theta} = -\frac{\frac{\omega_B^2}{\nu^2}\frac{E_z}{B_r}}{1+\frac{\omega_B^2}{\nu^2}} - \frac{\frac{\omega_B^2}{\nu^2}\frac{k_B T_e}{eB_r}\frac{1}{n_e}\frac{\partial n_e}{\partial z}}{1+\frac{\omega_B^2}{\nu^2}} \tag{21.c}$$

in order to take into account the transverse electron mobility (the electron-neutral collision frequency is set equal to $\nu=2.5x10^{13}n_{Xe}$) and diffusivity, while the radial magnetic field is done by the dipolar approximation:

$$B_r(r,z) = B_0\frac{\sin 2\theta}{(r^2+z^2)^{3/2}}. \tag{21.d}$$

After calculating the electron density one can solve the more detailed electron energy conserving equation for the temperature which, neglecting the unsteady and convection terms, assumes the following form:

$$\kappa_e \nabla^2 T_e + \nabla \kappa_e \cdot \nabla T_e = -Q_e . \tag{22.a}$$

The ionization energy sink term $Q_e = \dot{n}_e I$ is calculated using the volumetric ionization rate:

$$\dot{n}_e = k_{T_e} n_e n_{Xe} \tag{22.b}$$

where the following expression for the electron impact ionization rate coefficient is used[84]:

$$\begin{aligned} k(T_e) = {} & 4.5243 \times 10^{-15} - 4.4952 \times 10^{-15} T_e + 1.1776 \times 10^{-15} T_e^2 \\ & - 2.5515 \times 10^{-17} T_e^3 - 2.3932 \times 10^{-18} T_e^4 + 9.7869 \times 10^{-20} T_e^5 \end{aligned} \tag{22.c}$$

The electron thermal conductivity κ_e is included by the following fitting formula[85]:

$$\kappa_e = A T_e^n \qquad \text{wit h} \begin{cases} A = 6.9 \times 10^{-12} & n = 5/2, \quad T_e \le 2eV \\ A = 2.08 \times 10^{-3} & n = 1/2, \quad T_e > 2eV \end{cases} . \tag{22.d}$$

For electron temperatures below roughly *2 eV*, electron-ion collision are dominant, and *n=5/2* since $\kappa_e \sim T_e/\nu_{ei}$ and $\nu_{ei} \sim T_e^{-3/2}$. For electron temperatures above *2 eV*, electron-neutral collisions are dominant: since $\kappa_e \sim T_e/\nu_{en}$ and $\nu_{en} \sim \sqrt{T_e}$, one has *n=1/2*. eqs. (21-22) are iterated until the whole convergence is attained.

III. Results and Discussion

The convergence of PIC simulation is checked controlling the average total (potential + kinetic) energy of macroparticles. All the profiles shown are averaged over a few tens of plasma oscillation periods.

A. 2D(r,z) discharge: acceleration mechanism

First of all, we have verified that the output data follow the theoretical scaling laws of the self-similar system reported in Tab. I. A series of simulations using different values of the scaling parameter ζ have been performed. The behaviour is in good agreement with the theoretical prevision until a scaling factor equal to *1/200*. In fact, a small deviation from the theoretical scaling law is present for values smaller than *0.01*, proofing that surface, turbulence and numerical effects become important. In particular, Fig. 5 shows the axial profiles of plasma potential, electron density and electron temperature for two different values of scaling parameter (*0.01* and *0.1*). As it is evident, the behaviour does not change. From Fig. 5(a), also the little anode drop (*~40 V*) is evident.

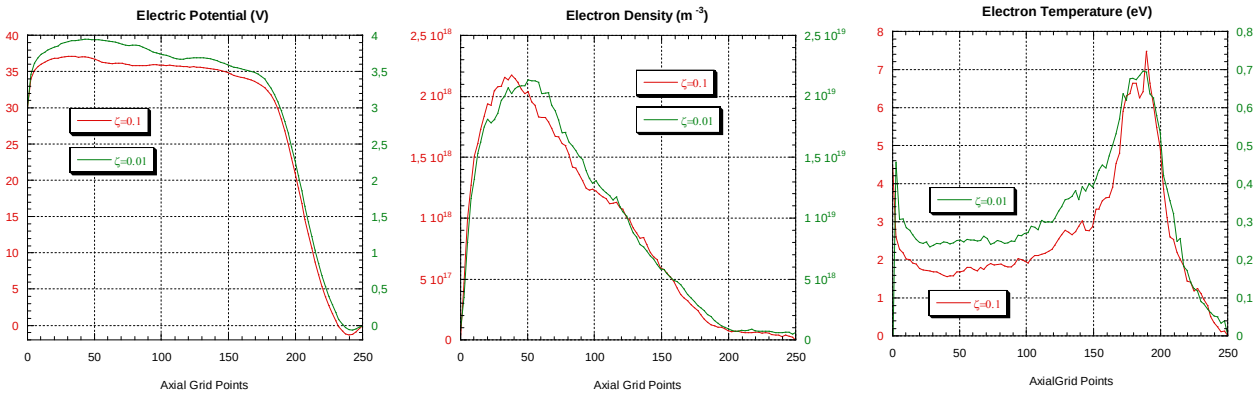

Figure 5. Axial profile of (a) plasma potential, (b) electron density and (c) electron temperature using two different scaling factor. The values are scaled.

The contour plots of Figs. 6 demonstrate the main features of the discharge. In particular, Figures 6(a) and 6(b) show, respectively, the space variation of the electric potential and ion density using a geometrical reducing factor $\zeta=1/50$. As it can see in Fig. 6(a), most of the potential drop occurs in the exhaust region, where the magnetic field is large. This decrease compensates the low electron conductivity in this region and ensures current continuity. It is customary to allocate the acceleration region here. The large axial electric field resulting from this voltage drop is responsible for accelerating the ions from the ionization region to the exit plane and the electron from the outlet to the anode. It can also be seen that equipotential lines are curved resulting from the equipotentialization of the magnetic field lines. However, the computed potential vanishes at the channel exit, while observations[86] indicate that only *1/2* to *1/3* of the potential drop takes place downstream of the thruster exit. This difference is due imposing the zero potential boundary condition at the exit plane in the numerical simulation (eq. (11.c)), i.e., the full potential drop is forced to occur inside the channel. The space variation of the plasma density (Fig. 6(b)) shows that the plasma reaches its maximum in the center of the channel and in the ionization region, while it decreases in the acceleration region due to the increasing ion velocity.

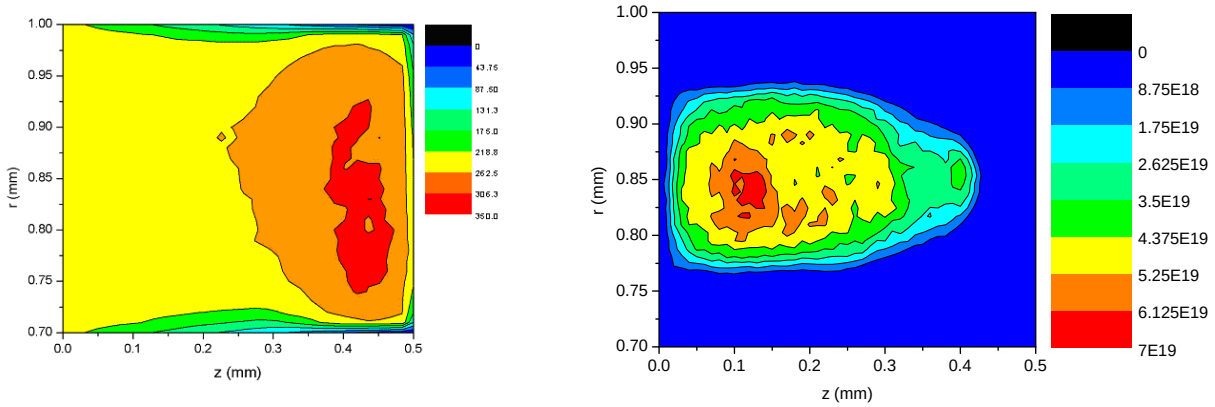

Figure 6. Colour plots of electric potential (V) and ion number density (m^{-3}) at steady-state.

One of the most important quantities visualizing ion dynamics is the ion current. Fig. 7(a) describes the ion streamlines, whereas Fig. 7(b) shows the ion scatter plot in the velocity space (v_z,z). The division into three distinct regions is evident. In the anode region, a backflow towards the anode exists due to the anode drop. Often this region is also called diffusion region due to the very low magnetic field. It ends with the transition towards a positive ion velocity, where the ionization zone begins. Finally, the separation between ionization and acceleration regions is located at the sonic transition. From Fig. 7(a) the importance of the ion flow towards the walls can be understood. In the ionization region the ions hit almost normal to the surface, while in the acceleration region the mean angle θ between ion velocity and surface normal increases up to a maximum value of *45°*. This is due to two concurrent effects: the reduction of the lateral sheath voltage in the acceleration region and the focusing effect of the convex magnetic field lines.

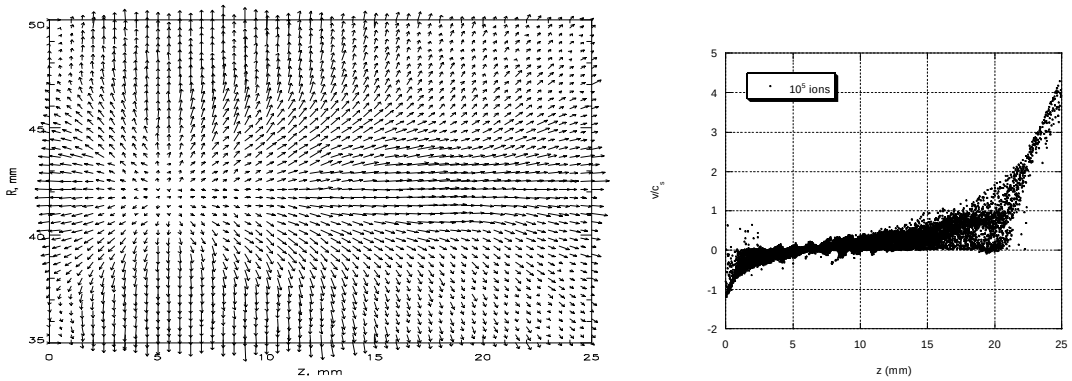

Figure 7. Ion current density vector plot and ion scatter plot in the phase space (v_z,z). Ion velocity is normalized to the ion sonic speed.

From the simulation results, the energy of ions impinging on the walls may be considered constant along the channel with a value of *340 eV*. These information will be used as input data for the SPTRIMSD analysis. In fact, when the steady state is reached, we collect all the information concerning the ions impacting on the wall, that is the energy and the impact angle distributions. In Fig. 8(a) the projection of trajectories (projectiles and recoils) in a plane normal to the surface for bombardment at $\theta=45°$ is shown. These plots give a good impression of what the code is doing and how particles move. The trajectories of projectiles are represented in black, while those of recoils are in red. The distribution of the end points of the trajectories give the depth profile, the lateral spread of the implanted particles and the sputtering yield. Finally, the code is able to calculate the ion distributions (radial position, energy and divergence angle) on the exit plane (Fig. 8(b)) which is an important information for analyzing the performance of the thruster and is used also as input data for plume simulations.

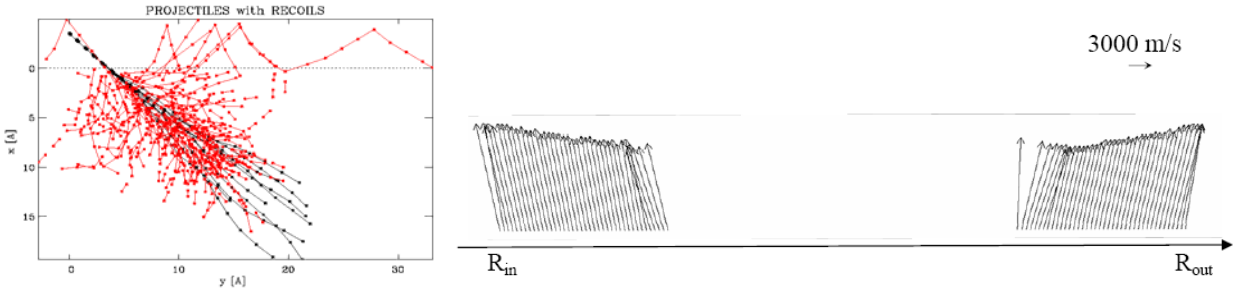

Figure 8. (a) Projection of projectile (black lines) and recoils (red lines) trajectories in a plane normal to the surface for the bombardment of BN by 340 eV Xe ions at θ=45°. (b) Arrows plot of the ion velocity on the exit plane of the channel.

B. 1D(r) acceleration region: microinstability

In Fig. 9(a), the radial profiles of the plasma potential is shown using two different value of axial electric field E_z (*100* and *300 V/cm*), while BN is used as wall material. The *E*-field represents the order parameter driving the transition between a stable and an unstable regime. In particular, at high *E* value, we have obtained that:

a) the potential drop in the pre-sheath is not negligible at all and can reach a value of *1/5* of the total potential drop, while the sheath drops is highly reduced;

b) the profiles of the inner and outer regions are asymmetrical: the potential peak moves towards the inner wall. The potential difference between inner and outer wall can reaches a value of *8 V*;

c) a space charge saturated regime with a double layer structure is present on the outer sheath;

d) a dynamically unstable regime appears. The plasma is no more insulated from the walls and a larger electron flux to the wall is present with consequent increased secondary electron flux which is accelerated toward the bulk.

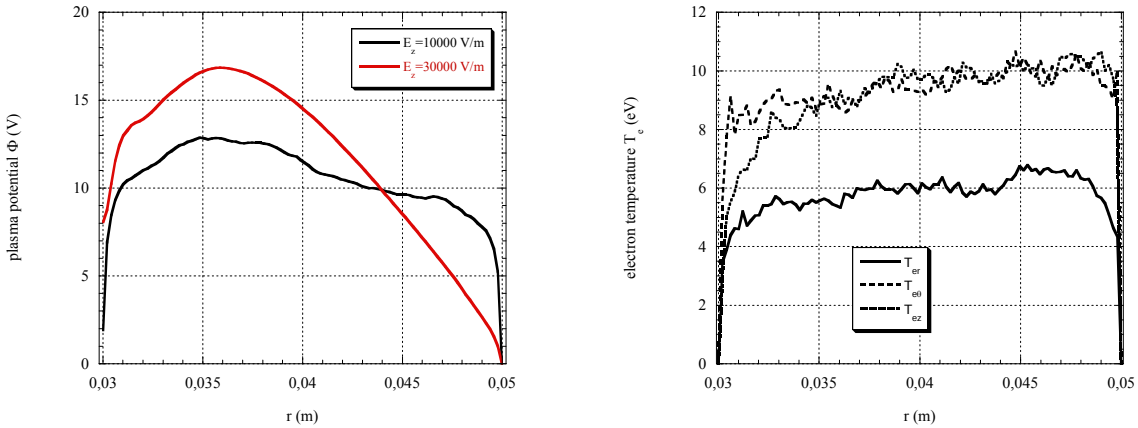

Figure 9. Radial profile of (a) plasma potential and (b) electron temperatures in the acceleration region.

In fact, as Fig. 10(a) shows the eedf is no more monotonic (the Penrose marginal stability criterion is fulfilled) and a beam-plasma instability appears. This local distortion of the eedf leads to the growth or decay of critical oscillatory modes[19,74] that can have an important effect on the azimuthal fluctuations and anomalous transport. In fact, a strong correlation between radial electric field instability and azimuthal electron drift energy fluctuations has been revealed. Finally, the typical beam-plasma instability vortex in the velocity space has been observed (Fig. 10(b)).

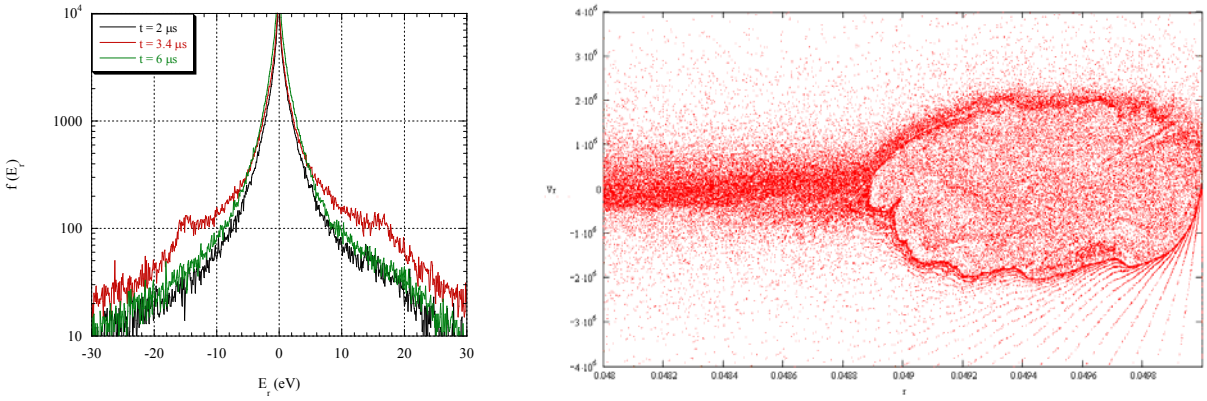

Figure 10. (a) eedf at three different time and electron scatter plot in the velocity space (v_r,r) near the outer wall at t=3.4 µs, that is during the instability.

The electron temperatures profile are shown on Fig. 9(b). The cooling effect of the secondary electrons emitted from the wall causes a pronounced anisotropic behaviour. The radial electron temperature is *4 eV* lower than the axial and azimuthal ones.

A non-trivial structure of the nascent near-wall current is revealed. In Fig. 11 the radial profile of the axial electron density current is depicted. The appearance of an oscillatory structure in the radial profile of axial current is the characteristic signature of near-wall conductivity, which distinguishes it from the classical bulk conductivity transverse to the magnetic field. These profiles can be interpreted as follows: secondary electrons initially tend to move against E_z due to the electrostatic force, but become as soon involved in a cycloidal motion due to the magnetic field and their axial velocity thus changes along the radial direction. Due to the randomness of the initial radial velocities, the phase of the different electrons becomes uncorrelated away from the walls and their respective contributions to the main axial velocity eventually cancel. The wall conduction layer is most pronounced near the outer wall of the channel and it is less defined near the inner ceramic. The most likely reason for this difference in behaviour of $j_{e,z}(r)$ is due to a magnetic mirror effect as a consequence of the *1/r* variation of the radial magnetic field (eq. (9)), or it could be also an annular effect (cylindrical metrics).

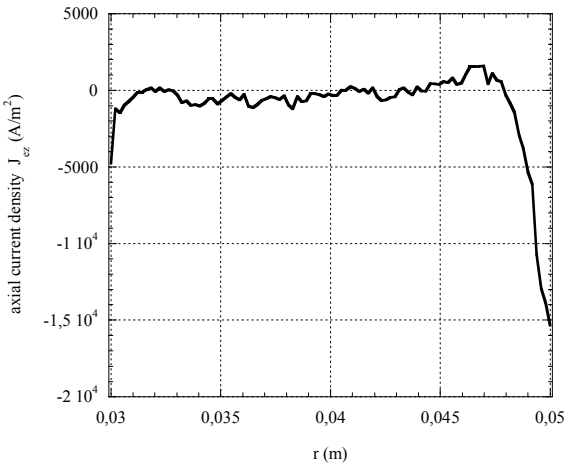

Figure 11. Radial profile of electron axial density current.

C. 2D(r,θ) acceleration region: azimuthal fluctuations

Fig. 12 shows the entire history plot of the plasma potential measured at a single point *(r,θ)=(0.04 m, 0.13 rad)* in the simulation domain, using E_z*=100 V/cm*. After an initial transient time (*~1 µs*), a burst of high amplitude

oscillations appears. It saturates and disappears after about *3 μs*, when a quiescent interval of *2 μs* anticipates a small amplitude oscillations period.

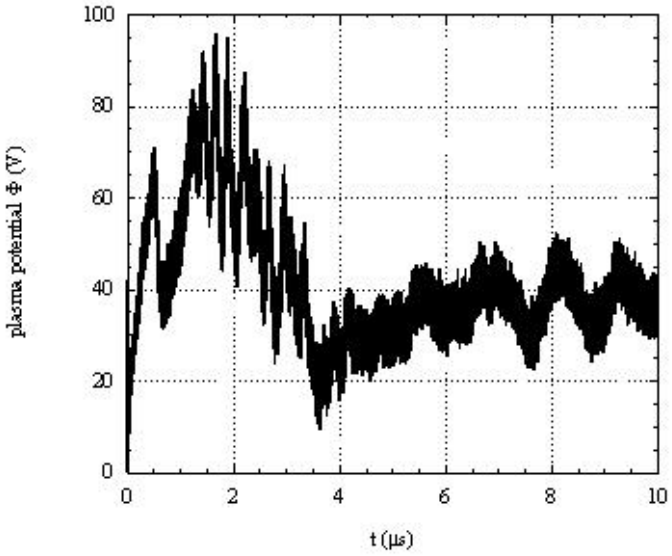

Figure 12. Time evolution of the plasma potential measured at a single point (r,θ)=(0.04 m, 0.13 rad) with Ez=100 V/cm.

Fig. 13(a) show the 2D(r,θ) distribution of the plasma potential at *t=1.5 μs*, that is during the strong burst. The azimuthal fluctuations are characterized by a wave number $k_\theta=80\ m^{-1}$, with a frequency of about *2.8 MHz*. The strong interaction with the walls is the most plausible candidate to excite this instability. Indeed, the sheath potential drop is azimuthally modulated, as the wall potential and the surface charge density. In fact, the combination of a reduced sheath (due to secondary electron emission) and a floating wall (non-linear coupling between current collected and wall potential eq. (14.b)) is the most important candidate to drive the azimuthal instability. The azimuthal fluctuation is not a standing wave, but it propagates with a phase velocity of about $5x10^4\ m/s$, as shown in Fig. 13(b). It represents the time evolution of the azimuthal profile of the plasma potential calculated at the radial center of the coaxial channel (*r=0.04 m*). It can be seen that, after an initial time of development, the plasma structure takes the shape of waves propagating with approximately constant phase velocity and with slightly increasing amplitude. Therefore, the spoke rotates at about $1/12(E_z/B_r)$ while the electrons in the spoke move at E_z/B_r. The resulting charge separation creates the azimuthal electric field which is correlated with the electron density. It has been speculated that the perturbation is driven from axial gradients[9] or from the out-of-axis cathode location[10]. In this work the azimuthal fluctuations exist even if these elements are absent in the simulation.

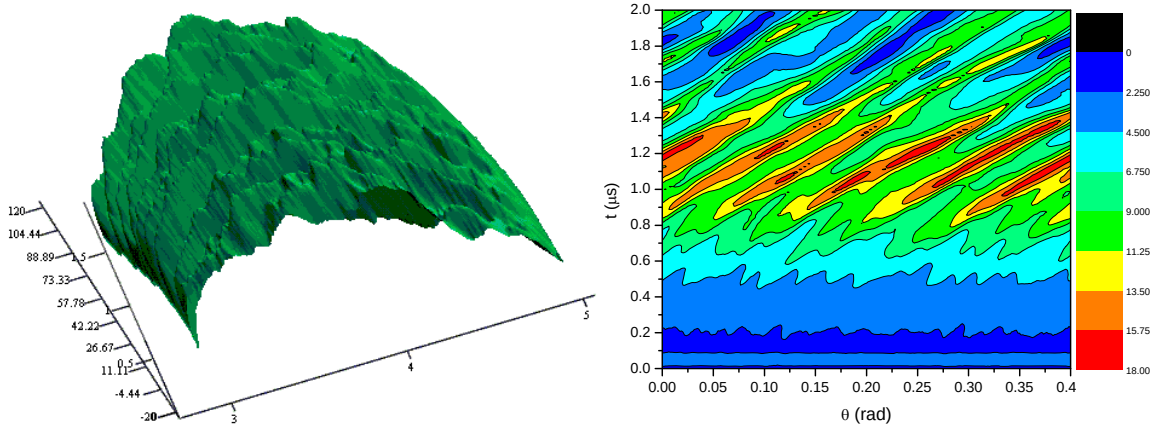

Figure 13. (a) Distribution of plasma potential (V) in the {r,θ} plane at t=1.5 μs. (b) Time evolution of the azimuthal profile of plasma potential (x10 V) calculated at r=0.04 m.

D. 2D(r,z) near- and far-field region

In Figs. 14(a) a snapshot is reported of the position of a limited number of marker ions during the simulation. Note that ions exit the thruster channel as a narrow beam with a divergency angle of about *40°* to the thruster axis and as a CX component out of the primary beam and propagating both up- and down-stream. Ions propagate under the effect of self-consistent electric field and collisions with neutrals until a stationary state is reached when the outflow balances the ion emission. Note that a significant component of backflow appears, as well as significant expansion in the radial direction. The effect of charge exchange collisions is clearly detectable in Fig. 14(b) that plots the (v_r-v_z) phase space at steady state. CX ions are visible as a wing of low velocity ions. Although CX ions begin with relatively low speed, the plume's potential structure tends to drive these ions sideways and backwards, towards the spacecraft rather than away from it.

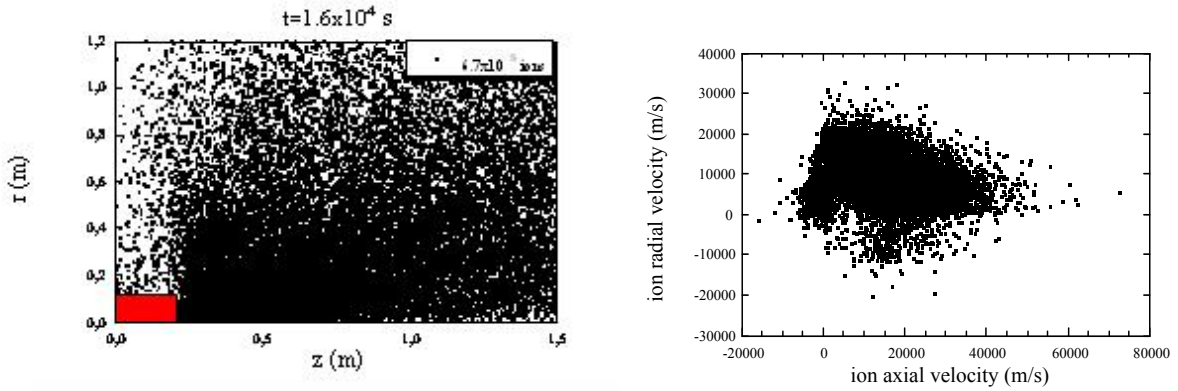

Figure 14. Phase space (r,z) and (v_r,v_z) plots of marker ions at the steady state.

Fig. 15 illustrates the electric potential at the steady state. We can note a fall of *~50 V* between the exit plane and the stagnation region, where a potential well develops spontaneously. The lobe structures seen directly on the side of the thruster exit are produced by the charge exchange plasma.

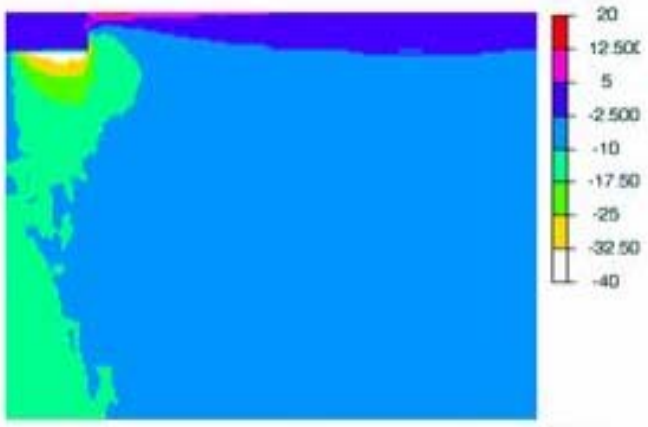

Figure 15. Color plot of the plume plasma potential (V) in the far-field region at the steady state.

Figure 16(a) shows the axial profiles of plasma potential in the near-field region. It is computed at two different radial positions, that is potential distribution across the magnetic field. One can see that at *r=0 mm* the potential at first increases as a function of the axial positions because electrons are trapped by the magnetic field effect and later decreases, since the value of magnetic field becomes relatively weak. At *r=20 mm* the magnetic field is substantially lower and the plasma potential increase is less marked. Figure 16(b) shows the radial profiles of the plasma potential calculated at two different axial positions, that is potential distribution along the magnetic field. The plasma potential decreases as the electron density according to the Boltzmann relation (16). Finally the overall behaviour of

the plasma potential is reported in Figure 16(c). One can see the potential wall structure developing spontaneously (for $d=\sqrt{(r^2+z^2)}<0.04\ m$) to capture ions apt to neutralize those electrons which are trapped by magnetic field.

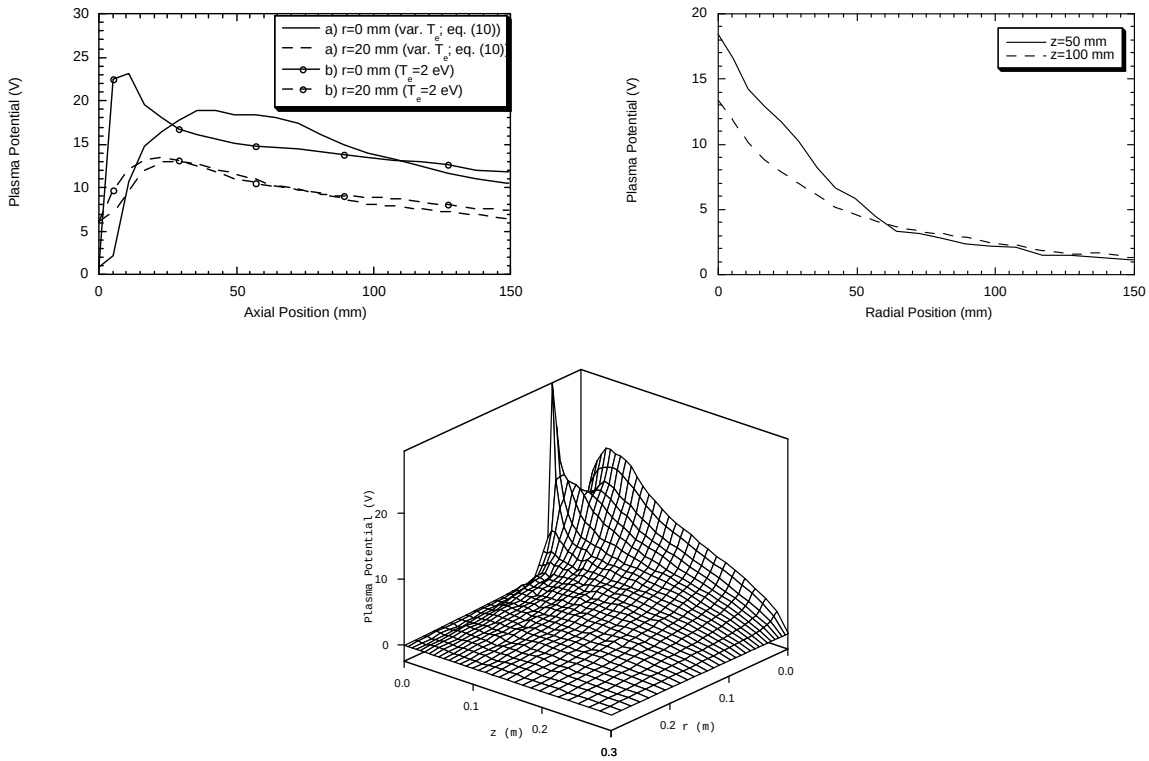

Figure 16. Plot of the plasma potential in the near-field region reported (a) as a function of axial position for different radial positions, (b) as a function of radial position, for different axial positions and (c) as surface plot in the (r,z) plane.

The radial distributions of ion current density measured at different axial positions are displayed in Fig. 17. The variation of the ion current density with axial distance from the thruster indicates that the ion flow begins as an annulus, and then merges into a single-body beam. Moreover on centreline (*r=0 mm*) the ion current density increases with axial positions lower than *z=100 mm* and then begins to decrease. This behaviour is attributed to the fact that the diverging annular ion beam overlaps at the centreline of the thruster with an angle of inner boundary of *16°* in accord with experimental measurements[81]. The discrepancy between model and experimental values in the low radial (*r<3 mm*) and axial (*z=10 mm*) positions is probably due to the effect of electron neutralizer position.

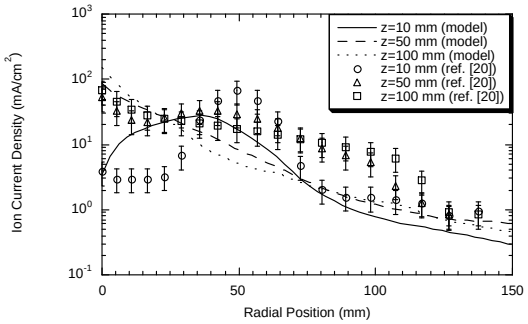

Figure 17. Plot of the steady state ion charge density, as a function of radial position, for different axial positions. Numerical results are compared with experimental results after Ref. 81.

IV. Conclusion

Different *ab-initio* PIC-MCC models of SPT-100 have been developed during the last seven years as a collaboration between IMIP-CNR of Bari (Italy) and the plasma edge group of the stellarator theory division of the Max-Planck Institute für Plasmaphysik of Greifswald (Germany). In particular, a detailed representation of plasma-wall interaction inside the acceleration channel and ion-neutral collision in the plume emitted from the thruster have made possible to better understand the physics involved in this device.

Acknowledgments

This work is supported by MIUR-PRIN 2005 under the contract n. 2005039049_005: "Dinamica dei processi elementary per la chimica e la fisica dei plasmi". R. S. acknowledges funding of the work by the Initiative and Networking Fund of the Helmholtz Association.

References

[1]Zhurin, V. V., Kaufman, H. R., and Robinson, R. S., "Physics of closed drift thruster," *Plasma Sources Sci. Technol.*, Vol. 8, 1999, pp. R1-R20.

[2]Hobbes, G. D., and Wesson, J. A., "Heat flow through a Langmuir sheath in the presence of electron emission," *Plasma Phys.*, Vol. 9, 1967, pp. 85-87.

[3]Kirdyashev, K. P., "Near-wall electron instability of a plasma flux," *Tech. Phys. Lett.*, Vol. 23, No. 5, 1997, pp. 395-396.

[4]Morozov, A. I., and Savel'ev, V. V., "Kinetics of a Low-Density Plasma near a Dielectric Surface with Account for Secondary Electron Emission", *Plasma Phys. Rep.*, Vol. 33, No. 1, 2007, pp. 20-27.

[5]Drummond, W. E., and Rosenbluth, M. N., "Anomalous diffusion arising from microinstabilities in a plasma," *Phys. Fluids*, Vol. 5, No. 12, 1962, pp. 1507-1513.

[6]Spitzer, L. Jr., "Particle diffusion across a magnetic field," *Phys. Fluids*, Vol. 3, 1960, pp. 659-661.

[7]Janes, G. S., and Lowder, R. S., "Anomalous electron diffusion and ion acceleration in a low-density plasma," *Phys. Fluids*, Vol. 9, No. 6, 1966, pp. 1115-1123.

[8]Esipchuck, Y. V., and Tilinin, G. N., "Drift instability in a Hall-current plasma accelerator", *Sov. Phys. – Tech. Phys.*, Vol. 21, 1976, pp. 419.

[9]Litvak, A. A., Raitses, Y., and Fisch, N. J., "Experimental studies of high-frequency azimuthal waves in Hall thrusters," *Phys. Plasmas*, Vol. 11, No. 4, 2004, pp. 1701-1705.

[10]Lazurenko, A., Albaréde, L., and Bouchoule, A., "Physical characterization of high-frequency instabilities in Hall thrusters," *Phys. Plasmas*, Vol. 13, 2006, 083503.

[11]Lazurenko, A., Dudok deWit, T., Cavoit, C., Krasnoselskikh, V., Bouchoule, A., and Dudeck, M., "Determination of the electron anomalous mobility through measurements of turbulent magnetic field in Hall thrusters," *Phys. Plasmas*, Vol. 14, 2007, 033504.

[12]Hirakawa, M., and Arakawa, Y., "Particle simulation of plasma phenomena in Hall thrusters," *Proceedings of the 24th International Electric Propulsion Conference*, IEPC-95-164, Moscow, Russia, 1995.

[13]Hirakawa, M., and Arakawa, Y., "Numerical simulation of plasma particle behavior in a Hall thruster," *Proceedings of the 32nd AIAA/ASME/SAE/ASEE Joint Propulsion Conference*, AIAA-96-3195, Lake Buena Vista, FL, 1996.

[14]Choueiri, E. Y., "Plasma oscillations in Hall thrusters," *Phys. Plasmas*, Vol. 8, No. 4, 2001, pp. 1411-1426.

[15]Litvak, A. A., and Fisch, N. J., "Resistive instability in Hall current plasma discharge," *Phys. Plasmas*, Vol. 8, No. 2, 2001, pp. 648-651.

[16]Litvak, A. A., and Fisch, N. J., "Rayleigh instability in Hall thrusters," *Phys. Plasmas*, Vol. 11, No. 4, 2004, pp. 1379-1383.

[17]Gallardo, J. M., and Ahedo, E., "On the anomalous diffusion mechanism in Hall-effect thrusters," *Proceedings of the 29th International Electric Propulsion Conference*, IEPC-2005-117, Princeton, NJ, 2005.

[18]Thomas, C. A., and Cappelli, M. A., "Fluctuation-induced transport in the Hall plasma accelerator," *Proceedings of the 42nd AIAA/ASME/SAE/ASEE Joint Propulsion Conference*, AIAA-2006-5168, Sacramento, CA, 2006.

[19]Ducrocq, A., Adam, J. C., Héron, A., and Laval, G., "High-frequency electron drift instability in the cross-field configuration of Hall thrusters," *Phys. Plasmas*, Vol. 13, 2006, 102111.

[20]Sydorenko, D., Smolyakov, A., Kaganovich, I., and Raitses, Y., "Effects of non-Maxwellian electron velocity distribution function on two-stream instability in low-pressure discharges,"*Phys. Plasmas*, Vol. 14, 2007, 013508.

[21]Yoshikawa, S., and Rose, D., "Anomalous diffusion of plasma across a magnetic field", *Phys. Fluids*, Vol. 5, 1962, pp. 334-340.

[22]Bohm, D., *The characteristics of electrical discharges in magnetic fields*, ch. 2, p. 65, McGraw-Hill, New York, 1949.

[23]Morozov, A. I., and Savelyev, V. V., in *Reviews of Plasma Physics*, edited by B. B. Kadomtsev and V. D. Shafranov, Consultants Bureau, New York, 2000, Vol. 21, pp. 277-299.

[24]Kaganovich, I. D., Raitses, Y., Sydorenko, D., and Smolyakov, A., "Kinetic effects in a Hall thruster discharge," *Phys. Plasmas*, Vol. 14, 2007, 057104.

[25]Wu, Z.-W., Yu, D.-R., and Wang, X.-G., "Effect of erosion surface on near wall conductivity (NWC) in the Hall-type stationary plasma thrusters," *Vacuum*, Vol. 80, 2006, pp. 1376-1380.
[26]Ivanov, A. A., Ivanov, A. A. Jr., and Bacal, M., "Effect of plasma-wall recombination on the conductivity in Hall thrusters," *Plasma Phys. Control. Fusion*, Vol. 44, 2002, pp. 1463-1470.
[27]Barral, S., Makowski, K., Peradzyński, Gascon, N., and Dudeck, M., "Wall material effects in stationary plasma thrusters. II. Near-wall and in-wall conductivity," *Phys. Plasmas*, Vol. 10, No. 10, 2003, pp. 4137-4152.
[28]Yu, D., Li, H., Wu, Z., and Mao, W., "Effect of oscillating sheath on near-wall conductivity in Hall thrusters," *Phys. Plasmas*, Vol. 14, 2007, 064505.
[29]Boniface, C., Garrigues, L., Hagelaar, G. J. M., Boeuf, J. P., Gawron, D., and Mazouffre, S., "Anomalous cross field electron transport in a Hall thruster," *Appl. Phys. Lett.*, Vol. 89, 2006, 161503.
[30]Gascon, N., Dudeck, M., and Barral, S., "Wall material effects in stationary plasma thrusters. I. Parametric studies of an SPT-100," *Phys. Plasmas*, Vol. 10, No. 10, 2003, pp. 4123-4136.
[31]Raitses, Y., Smirnov, A., Staack, D., and Fisch, N. J., "Measurements of secondary electron emission effects in the Hall thruster discharge," *Phys. Plasmas*, Vol. 13, 2006, 014502.
[32]Tahara, H., Imanaka, K., and Yuge, S., "Effects of channel wall material on thrust performance and plasma characteristics of Hall-effect thrusters," *Vacuum*, Vol. 80, 2006, pp. 1216-1222.
[33]Thomas, C. A., "Anomalous electron transport in the Hall-effect thruster", PhD Dissertation, Mechanical Engineering Dept., Stanford University, Stanford, California, 2006.
[34]Eastwood, J. W., and Hockney, R. W., *Computer Simulation using Particle*, McGraw-Hill, New York, 1981.
[35]Birdsall, C. K., and Langdon, A. B., *Plasma Physics via Computer Simulation*, McGraw-Hill, New York, 1985.
[36]Keidar, M., Boyd, I. D., and Beilis, I. I., "Plasma flow and plasma-wall transition in Hall thruster channel," *Phys. Plasmas*, Vol. 8, No. 12, 2001, 5315-5322.
[37]Choueiri, E. Y., "Fundamental difference between the two Hall thruster variants," *Phys. Plasmas*, Vol. 8, No. 11, 2001, pp. 5025-5033.
[38]Dorf, L., Semenov, V., and Raitses, Y., "Anode sheath in Hall thrusters," *Appl. Phys. Lett.*, Vol. 83, No. 13, 2003, pp. 2551-2553.
[39]Komurasaki, K., and Arakawa, Y., "Two-dimensional numerical model of plasma flow in a Hall thruster," *J. Prop.& Power*, Vol. 11, No. 6, 1995, pp. 1317-1323.
[40]Garrigues, L., "Modelisation d'un propulseur à plasma stationnaire pour satellites," PhD Dissertation, Université Paul Sabatier, Toulouse, 1998.
[41]Fife, . M., "Hybrid-PIC modelling and electrostatic probe survey of Hall thrusters," PhD Dissertation, Dept. of Aeronautics and Astronautics, Massachusetts Institute of Technology, Boston, New England, 1999.
[42]Koo, J. W., and Boyd, I. D., "Computational modelling of stationary plasma thrusters," *Proceedings of the 39th AIAA/ASME/SAE/ASEE Joint Propulsion Conference and Exhibit*, AIAA-2003-10113, Huntsville, Alabama, 2003.
[43]Latocha, V., "Deux problèmes en transport des particules chargées intervenant dans la modélisation d'un propulseur ionique", PhD Dissertation, Laboratoire Mathématiques pour l'Industrie et la Physique, Université Paul Sabatier, Toulouse, France, 2001.
[44]Szabo, J. J. Jr., "Fully kinetic numerical modeling of a plasma thruster", PhD Dissertation, Aeronautics and Astronautics Dept., Massachusetts Institute of Technology, Boston, New England, 2001.
[45]Taccogna, F., Plasma-wall interaction inside a Hall thruster, PhD Dissertation, Chemistry Dept. University of Bari, Italy, 2003.
[46]Taccogna, F., Longo, S., Capitelli, M., and Schneider, R., "Fully kinetic Particle-in-Cell simulation of a Hall thruster," *Lecture Notes in Computer Science*, Vol. 3039, 2004, pp. 588-595.
[47]Taccogna, F., Longo, S., Capitelli, M., and Schneider, R., "Stationary plasma thruster simulation," *Comp. Phys. Comm.*, Vol. 164, 2004, pp. 160-170.
[48]Taccogna, F., Longo, S., Capitelli, M., and Schneider, R., "Plasma flow in a Hall thruster," *Phys. Plasmas*, Vol. 12, 2005, 43502.
[49]Taccogna, F., Longo, S., Capitelli, M., and Schneider, R., "Multi-scale simulation of Hall discharge," *International Journal for Multiscale Computational Engineering*, Vol. 4, No. 2, 2006, pp. 243-254.
[50]Taccogna, F., Longo, S., Capitelli, M., and Schneider, R., "Start-up transient in a Hall thruster," *Contr. Plasma Phys.*, Vol. 46, No. 10, 2006, pp. 781-786.
[51]Taccogna, F., Longo, S., Capitelli, M., and Schneider, R., "Self-similarity in Hall plasma discharge. Application to particle models," *Phys. Plasmas*, Vol. 12, 2005, 053502.
[52]Adam J. C, Gourdin Serveniere A., and Langdon A. B., "Electron sub-cycling in particle simulation of plasmas," *J. Comp. Phys.* Vol. 47, 1982, pp. 229-244.
[53]Verboncoeur, J. P., "Symmetric spline weighting for charge and current density in particle simulation," *J. Comp. Phys.,* Vol. 174, 2001, pp. 421-427.
[54]Möller, W., and Eckstein, W., "TRYDIN – Binary collision simulation of atomic collisions dynamic composition changes in solids", Report n° IPP 9/64, Max-Planck-Institute für Plasmaphysik, Garching bei Munchen, Germany, 1988.
[55]Nanbu, K., "Probability theory of electron-molecule, ion-molecule, molecule-molecule, and coulomb collisions for particle modeling of materials processing plasmas and gases", *IEEE Trans. Plasma Sci.*, Vol 28, No. 3, 2000, pp. 971-.990.

[56]Vahedi, V., Surendra, M., "A Monte Carlo collision model for particle-in-cell method: applications to argon and oxygen discharges", *Comp. Phys. Comm.,* Vol. 87, 1995, pp. 179-198.
[57]Surendra, M., Graves, D. B., Morey, I. J., "Electron heating in low-pressure rf glow discharges," *Appl. Phys. Lett.*, Vol. 56, No. 11, 1990, pp. 1022-1024.
[58]Taccogna, F., Longo, S., and Capitelli, M., "Plasma-surface interaction model with secondary electron emission effects," *Phys. Plasmas*, Vol. 11, No. 3, 2004, pp. 1-7.
[59]Taccogna, F., Longo, S., and Capitelli, M., "Effect of secondary electron emission from a floating surface on the plasma sheath," *Vacuum*, Vol. 73, 2004, pp. 89-92.
[60]Taccogna, F., Longo, S., and Capitelli, M., "Plasma sheaths in Hall discharge," *Phys. Plasmas* 12, 2005, 093506.
[61]Taccogna, F., Longo, S., and Capitelli, M., "Numerical Model of Plasma sheaths in Hall Thruster," *Proceedings of the 29th International Electric Propulsion Conference*, IEPC-2005-12, Princeton, NJ, 2005.
[62]Taccogna, F., Schneider, R., Longo, S., and Capitelli, M., "Effect of surface roughness on secondary electron emission in a Hall discharge," *Proceedings of the 42nd AIAA/ASME/SAE/ASEE Joint Propulsion Conference*, AIAA-2006-4662, Sacramento, CA, 2006.
[63]Press, W. H., Teukolsky, S. A., Vetterling, W. T., and Flannery, B. P., *Numerical Recipes in Fortran 77: The Art of Scientific Computing*, Cambridge University Press, New York, 2001. Available online, http://www.nr.com.
[64]Furman, M. A., Pivi, M. T. F., "Probabilistic model for the simulation of secondary electron emission", *Phys. Rev. Special Topics–Accel. and Beams*, Vol. 5, 2002, 124404.
[65]Cimino, R., Collins, I. R., Furman, M. A., Pivi, M., Ruggiero, F., Rumolo, G., and Zimmermann, F., "Can low-energy electrons affect high-energy physics accelerators?," *Phys. Rev. Lett.*, Vol. 93, No. 1, 2004, 014801.
[66]Dennison, J. R., Sim, A., and Thomson, D., "Evolution of the electron yield curves of insulators as a function of impinging electron fluence and energy," *IEEE Trans. Plasma Sci.*, Vol. 34, No. 5, 2006, pp. 2204-2218.
[67]Clerc, S., Dennison, J. R., Hoffmann, R., and Abbott, J., "On the computation of secondary electron emission models," *IEEE Trans. Plasma Sci.*, Vol. 34, No. 5, 2006, pp. 2219-2225.
[68]Shih, A., and Hor, C., "Secondary emission properties as a function of the electron incidence angle," *IEEE Trans. Electr. Dev.*, Vol. 40, No. 4, 1993, pp. 824-829.
[69]Dawson, P. H., "Secondary electron emission yields of some ceramics," *J. Appl. Phys.*, Vol. 37, 1966, pp. 3644-3645.
[70]Bugeat, J. P., and Koppel, C., "Development of a Second Generation of SPT," *Proceedings of the 23rd International Conference on Electric Propulsion,* IEPC 95-35, Moscow, Russia, 1995.
[71]Dunaevsky, A., Raitses, Y., and Fisch, N. J., "Secondary electron emission from dielectric materials of a Hall thruster with segmented electrodes," *Phys. Plasmas*, Vol. 10, No. 6, 2003, pp. 2574-2577.
[72]Adam, J. C., Héron, A., and Laval, G., "Study of stationary plasma thrusters using two-dimensional fully kinetic simulations," *Phys. Plasmas*, Vol. 11, No. 1, 2004, pp. 295-305.
[73]Fernandez, E., Knoll, A., and Cappelli, M. A., "An axial-azimuthal hybrid simulation of coaxial Hall thrusters," *Proceedings of the 42nd AIAA/ASME/SAE/ASEE Joint Propulsion Conference*, AIAA-2006-4329, Sacramento, CA, 2006.
[74]Meezan, N. B., "Electron transport in a coaxial Hall discharge," PhD Dissertation, Mechanical Engineering Dept., Stanford University, Stanford, California, 2002.
[75]Taccogna, F., Schneider, R., Longo, S., and Capitelli, M., "Fully kinetic 2D(r,θ) model of a Hall discharge," *Proceedings of the 43rd AIAA/ASME/SAE/ASEE Joint Propulsion Conference*, AIAA-2006-5211, Cincinnati, OH, 2007.
[76]Swarztrauber, P. N., "A direct method for the discrete solution of separable elliptic equations," *SIAM J. Numer. Anal.*, Vol. 11, No. 6, 1974, pp. 1136-1150. See also: http://www.cisl.ucar.edu/css/software/fishpack/.
[77]F. Taccogna, S. Longo, M. Capitelli, "Particle in Cell/Monte Carlo model of the SPT-100 plume," Technical report No. WP 6.2 "Advanced prediction methods for plume flows", ESA/ESTEC contract n. 12736/97/NL/PA, May 2000.
[78]Taccogna, F., Longo, S., and Capitelli, M., "Particle in Cell/Monte Carlo Model of an electric thruster," *Proceedings of the 31st AIAA Plasmadynamics and Lasers Conference*, AIAA-2000-2345, Denver, CO, 2000.
[79]F. Taccogna, S. Longo, M. Capitelli, "Particle-in-Cell with Test-Particle Monte Carlo (PIC/TPMC) Simulation of SPT-100 Exhaust Plumes," *J. Spac. & Rock.*, Vol. 39, No. 3, 2002, pp. 409-419.
[80]Boccaletto, L., "Electric thruster technologies SPT-100 ion inflow data," Technical report No. WP-3 ESA/ESTEC 12736/97/NL/PA, December 1999.
[81]Kim, S. W., "Experimental investigation of plasma parameters and species-dependent ion energy distribution in the plasma exhaust plume of a Hall thruster," PhD Dissertation, University of Michigan, Departement of Areospace Engineering, 1999.
[82]Nanbu, K., Kitatani, Y., "An ion-neutral species collision model for particle simulation of glow discharge", *J. Phys. D: Appl. Phys.*, Vol. 28, 1995, pp. 324-330.
[83]Taccogna, F., Longo, S., and Capitelli, M., "Very-near-field plume simulation of a stationary plasma thruster," *Europ. Phys. J., Appl. Phys.*, Vol. 28, 2004, pp. 113-122.
[84]Colonna, G., Pietanza, L. D., and Capitelli, M., *Proceedings of the 31stAIAA Plasmadynamics and Lasers Conference*, AIAA-2000-2349, Denver, CO, 2000.
[85]Samanta Roy, R. I., "Numerical simulation of ion thruster plume backflow for spacecraft contamination assessment," PhD Dissertation, Aeronautics and Astronautics Dept., Massachusetts Institute of Technology, Boston, New England, 1995.
[86]Haas J. M., and Gallimore A. D., *Phys. Plasmas* Vol. 8, No. 2, pp. 652-, 2001.